RSC Advances

PAPER

View Article Online
View Journal | View Issue

Cite this: *RSC Adv.*, 2024, **14**, 5184

Highly efficient Fe–Cu dual-site nanoparticles supported on black pearls 2000 (carbon black) as oxygen reduction reaction catalysts for Al–air batteries†

Kun Liu, Xiaoyue Ye, Angli Zhang, Xiaoyan Wang, Ting Liang, Yan Fang, Wang Zhang, Ke Hu, Xiaowu Liu * and Xin Chen *

Acquiring cost-effective, high-performance, non-precious metal catalysts is crucial for substituting precious metal catalysts in the oxygen reduction reaction (ORR) to ensure sustainable energy conversion. Herein, we present a preparation strategy for a high-performance Cu–Fe–CN-3 electrocatalyst characterized *via* X-ray diffraction (XRD), Raman spectroscopy, Brunauer–Emmett–Teller (BET), scanning electron microscopy (SEM), transmission electron microscopy (TEM), and X-ray photoelectron spectroscopy (XPS) analyses. The results demonstrated that the incorporation of Cu and Fe into Black Pearls' carbon black (BP2000) and the strong synergistic effect between Fe and Cu contributed to the enhancement of active sites for the ORR. Electrochemical characterization revealed that the Cu–Fe–CN-3 catalyst synthesized by mixing Cu and Fe in a molar ratio of 3 : 1 exhibits superior catalytic activity for the ORR. The ORR performance of the Cu–Fe–CN-3 catalyst in an alkaline electrolyte ($E_{1/2}$ 0.867 V *vs.* RHE) surpassed that of Pt/C ($E_{1/2}$ 0.841 V *vs.* RHE), and the assembled aluminum–air battery demonstrated superior voltage stability compared to Pt/C under the same current density. After 2000 cycles, the $E_{1/2}$ of the Cu–Fe–CN-3 catalyst exhibited a slight negative shift by 5 mV, which was better than the activity loss of the Pt/C catalyst (12 mV). At the same current density, the average discharge platform of Al–air batteries with the Cu–Fe–CN-3 catalyst was better than that of the commercial Pt/C catalyst. Therefore, the prepared Cu–Fe–CN-3 electrocatalyst exhibits great potential as an efficient ORR catalyst in fuel cells.

Received 23rd November 2023
Accepted 23rd January 2024

DOI: 10.1039/d3ra07925b

rsc.li/rsc-advances

Introduction

In the 1980s, aluminum–air batteries developed by the United States, Canada, and Norway were mainly used in navigation lights, deep-sea rescue boats, and unmanned underwater vehicles. With significant improvements in the specific energy of Al–air batteries, the first battery-powered car appeared in the United States in the 1990s.[1,2] In 2015, Alcoa and Israel-based Phinergy set the world record of 1600 kilometers for a racecar equipped with a 100 kilogram Al–air battery at Circuit Gilles Villeneuve in Montreal. In 2016, electric vehicles powered with the same weight of Al–air batteries covered more than 3000 kilometers.[3] Al–air batteries have received extensive attention owing to their advantages of high energy density, high energy efficiency, and low emission.[4,5] Despite these important advances, their commercial applications are still hampered by the slow kinetics of the oxygen reduction reaction (ORR) on the cathode.[6,7] In our previous research, we reported on the utilization of Co_3O_4–CeO_2/KB,[8] Co_3O_4/Co–N–C,[9] and Fe_3C@Fe/N catalysts[10] as positive electrode materials for Al–air batteries. These materials have demonstrated significant enhancements in electrocatalytic performance for the ORR at high current densities. Moreover, their voltage performance surpasses that of Pt/C as current density increases. The ORR is a critical reaction in sustainable energy conversion devices such as fuel cells and metal–air batteries.[11] At present, Pt-based materials are still the most popular ORR catalysts in terms of their catalytic activity and stability. However, the scarcity of platinum makes these catalysts expensive, thus hindering their further application. Therefore, the development of novel non-precious metal catalysts with excellent catalytic activity and stability in the ORR has become mainstream.[12–14]

In recent years, transition metal coordinated nitrogen carbon materials (M–N–C) have been considered potential ORR electrocatalysts to replace Pt-based catalysts owing to their good ORR properties.[15,16] Fe–N–C catalysts have attracted much attention, particularly because of the synthesis method being simple and cost-effective.[17] The conventional approaches to enhance the performance of Fe–N–C catalysts involve the careful selection of

Anhui Provincial Laboratory of Biomimetic Sensor and Detecting Technology, College of Materials and Chemical Engineering, West Anhui University, Lu'an 237012, China. E-mail: 22000024@wxc.edu.cn; cx810101@163.com; Fax: +86 0564 3305690; Tel: +86 0564 3305690

† Electronic supplementary information (ESI) available. See DOI: https://doi.org/10.1039/d3ra07925b

appropriate nitrogen and carbon sources, as well as the optimization of synthesis conditions.[18,19] Despite some significant progress, additional enhancements to the performance of Fe–N–C are imperative. The incorporation of Cu atoms improves the catalytic activity in the oxygen reduction reaction (ORR), and our interest lies in the unique properties exhibited by Cu compared to other transition metals such as Co, Ni, Mn, and Zn.[19,20] The positioning of Cu in close proximity to the summit of the volcano-plot suggests a theoretically elevated level of ORR activity. In fact, the strong complexation ability of copper with nitrogen atoms increases the doping level of nitrogen atoms. In addition, the presence of copper in various valence states (Cu(0), (Cu(I), Cu(II), and even Cu(IV))) could potentially impact the efficient electron transfer during electrocatalysis.[1,21] The incorporation of Cu atoms as an accelerator in Fe–N–C catalysts has generated significant interest for the aforementioned reasons.

The synergistic effect of Fe and Cu significantly mitigates the release of reductive oxygen toxicity, thereby reducing the detrimental effects of the Fenton reaction and enhancing the stability of membrane electrode.[22,23] The selectivity of co-doped catalysts containing Fe and Cu is significantly enhanced in ORR compared to that of similar iron-based catalysts, and the former exhibiting less than one-third H_2O_2 yield of the latter.[24,25] Can bimetallic catalysts of Fe/Cu overcome the limitations of ORR catalysts? In recent years, researchers have synthesized a large number of Cu and Fe co-doped carbon materials exhibiting exceptional electrocatalytic activity.[26,27] However, the catalytic mechanism underlying iron and copper bimetallic catalysts remains elusive.[28,29] By manipulating the active center of the metal, the overall catalytic efficiency of the single atom electrocatalyst relies not only on the intrinsic activity of the M–N_x active site but also on the electrochemical accessibility of individual atoms. Consequently, efforts have been made to enhance the loading of metal atoms in the precursor, which undergoes conversion into a carbon carrier with a high-density distribution of isolated single atoms, thereby synergistically enhancing electrochemical activity.[30,31] We present a highly active electrocatalyst (Cu–Fe–CN-3) with Fe and Cu co-doped for ORR in alkaline electrolytes. Specifically, the pre-treated Black Pearls' carbon black is mixed with iron acetylacetone, copper acetylacetone, dimethylimidazole, and zinc nitrate. After the reaction, the initial catalyst product was obtained by filtration. Subsequently, the mixture undergoes pyrolysis and pickling to eliminate unstable metal compounds. Finally, Fe and Cu bimetal co-doped carbon-based catalysts were obtained. The incorporation of Cu dopant into the Fe–N–C catalyst leads to a significant enhancement in both ORR activity and durability. In alkaline media, Cu–Fe–CN-3 exhibits a half-wave potential ($E_{1/2}$) of 0.867 V, surpassing the performance of reference Pt/C catalysts with $E_{1/2}$ values of 0.841 V.

Experimental section

Chemicals and materials

Copper acetylacetonate ($Cu(C_5H_7O_2)_2$, 97%, Macklin), iron acetylacetonate ($Fe(C_5H_7O_2)_3$, 98%, Macklin), methanol (CH_3OH, ≥99.9%, Macklin), 2-methylimidazole ($C_4H_6N_2$, ≥98%, Macklin), ammonium chloride (NH_4Cl, 99.8%, Rhawn), sodium stannate trihydrate ($Na_2SnO_3 \cdot 3H_2O$, 98%, Heowns), indium hydroxide ($In(OH)_3$, 99.9%, Heowns), zinc oxide (ZnO, 99%, Macklin). The platinum/carbon (Johnson Matthey) with a weight percentage of 20% and potassium hydroxide (KOH, 95% McLean) with analytical grade (A.R.) purity were procured from Jiangsu Aikang Biopharmaceutical R&D Co., Ltd., China. Nitric acid (HNO_3, Xilon Technology), hydrochloric acid (HCl, 95%), and zinc nitrate hexahydrate ($Zn(NO_3)_2 \cdot 6H_2O$, ≥98%) were also analytical grade reagents purchased through unified bidding by West Anhui university. Ketjenblack carbon (EC300J) and acetylene black (Dedka Black Li-2060) were purchased from Tianjin Saibo Technology Co., Ltd., which were used as received without further purification steps in the experiments conducted. However, the BP2000 (Black Pearls 2000 carbon black, Cabot Corporation) utilized in our experiments necessitates additional processing, as detailed in the Key Materials synthesis section provided below. The mass ratio of the Nafion solution is 5 wt%, as provided by DuPont. Al alloy plate (industrial grade), Foam nickel (surface density 380 g m^{-2}), and waterproof breathable membrane were provided by Changzhou You Teke New Energy Technology Co., Ltd.

Synthesis of Cu–Fe–N–C@BP2000, Fe–N–C@BP2000, and Cu–N–C@BP2000

In our previous study, we reported that Fe–N–C electrocatalysts exhibit superior ORR activity compared to the commercial Pt/C (20 wt%).[10,32] As a continuation of our previous research, we have successfully synthesized highly active Fe–Cu two-site nanoparticles loaded on Black Pearls 2000 carbon black (Cu–Fe–N–C@BP2000) using copper acetylacetone, iron acetylacetone, 2-methylimidazole, and acid-treated carbon as raw materials for enhancing the reaction (ORR) in Al–air batteries (Fig. 1). 1.0 g of BP2000 was purified based on our previous description to eliminate other impurities and introduce functional groups on the carbon surface.[32] The above acid-treated carbon (0.1 g) was dispersed in methanol (50 mL) *via* an ultrasonic cleaning machine (KQ-50 ES, Kunshan ultrasonic instruments co., Ltd.) for 20 min, then 1.0421 g of 2-methylimidazole was added to the mixed suspension, followed by vigorously stirring for 30 min in the beaker to form uniform ink suspension, designated as A. Zinc nitrate hexahydrate (8.8789 g), copper acetylacetonate (0.8692 g), and iron acetylacetonate (0.2794 g) [the molar ratio of copper to iron is (3 : 1)] were

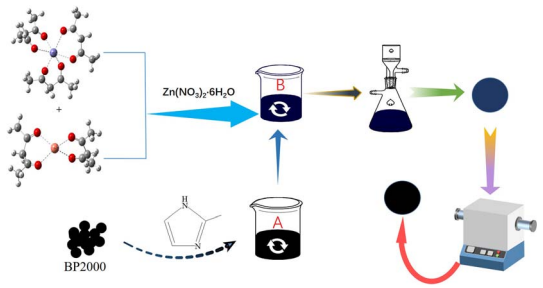

Fig. 1 Schematic of the synthesis procedure of Cu–Fe–NC-*X* (*X* = 1/3, 1/2, 1, 2, 3, and 4).

dissolved in 50 mL of methanol. Then, the above salt solution was strongly stirred for 6.0 h to form a homogeneous solution, designated as B. The A suspension was quickly poured into solution B and stirred at room temperature for 24 h. Finally, the Cu–Fe–N–C@BP2000 precursor was filtered and washed several times with anhydrous methanol and dried for 24 h under vacuum at 120 °C. Then, the dried Cu–Fe–N–C@BP2000 precursor and NH_4Cl at a mass ratio of 1 : 0.3 were ground in an agate mortar for 0.5 h, and pyrolyzed at 900 °C for 1 h in a tube furnace in an inert gas atmosphere. After that, the product was naturally cooled to room temperature, and the black powder was acid-treated with 0.1 M HNO_3 at 80 °C for 5 h to remove unstable nanoparticles. Next, the obtained black sample was filtered and dried overnight at 80 °C in a vacuum oven. The above sample was named as Cu–Fe–NC-3.

In order to optimize the electrocatalytic activity towards ORR, a series of comparative experiments, including different Cu/Fe molar ratios, whether to introduce iron or copper sources simultaneously, were also designed. The molar ratio of Cu/Fe was 4 : 1, 2 : 1, 1 : 1, 1 : 2, 1 : 3, and other synthesis conditions were consistent with those of Cu–Fe–NC-3, which were labeled as Cu–Fe–NC-4, Cu–Fe–NC-2, Cu–Fe–NC-1, Cu–Fe–NC-1/2, Cu–Fe–NC-1/3, respectively. Once the optimal molar ratio of Cu/Fe is determined, further investigation will be conducted to determine whether to add iron salt and copper salt separately, which are labeled as Fe–N–C and Cu–N–C. The follow-up procedures remain consistent with those for Cu–Fe–NC-3.

Material characterization

Crystallographic structures of the materials were investigated by an X-ray diffractometer (XRD, D8 Advance, Germany) with Cu-Kα radiation in a 2theta rotation range: 10° to 90°. A minimum readable step size of 0.0001° and angle reproducibility of 0.0001° were also required during testing. The angular deviation of all peaks in the full spectrum range is not more than ±0.01 degree. The microscopic size measurement, morphology characterization, and element distribution of the powders were detected using SEM (SU8010, Hitachi, Japan) with coupled energy dispersive spectrometry (EDS). The acceleration voltage was between 0.1 kV and 30 kV. High resolution transmission electron microscopy images of samples were captured by JEOL JEM-2100 with electron energy loss microspectroscopy. Raman spectroscopy was carried out on JOBIN YVON HR800 with a 532 nm laser source to detect the defects in samples. The chemical composition and states of samples were analyzed by X-ray photoelectron spectroscopy (XPS, ESCALAB 250 system with an Al Kα source). The metal composition of the final sample is accurately determined through inductively coupled plasma-atomic emission spectroscopy (ICP, Thermo Fisher iCAP 7400) analysis. Additionally, the surface area and pore size of the sample were calculated from N_2 sorption isotherms obtained on a Micromeritics Gemini 2380 surface analyzer.

Electrochemical measurements

The prepared catalyst (4 mg) was dispersed in 950 μL of ethanol and 100 μL of 5 wt% Nafion solution, followed by ultrasonic treatment for 20 minutes to achieve a homogeneous suspension. The 10 μL mixture drops were loaded onto the polished glass carbon electrode with a diameter of 5 mm as the working electrode, reference electrode, [Hg/HgO (1 M KOH)], and the counter electrode (platinum wire) to form a three-electrode system. Before measurement, the electrolyte is bubbled with high-purity O_2 for 30 minutes until saturated. The ORR performance of the sample in 0.1 M KOH solution saturated with O_2 was investigated using a rotating ring disk electrode (RRDE) and cyclic voltammetry (CV), and the entire measurement was carried out at the Ivium Electrochemical Station, Netherlands. The tests were performed at room temperature, and unless otherwise specified, all electrochemical tests were carried out with a scan rate of 10 mV s^{-1}. Within the voltage range of −1.0 to 0.2 V, the CV curve was scanned using the same scanning rate. The normalized area of the catalyst used (expressed in mA cm^{-2}) was obtained from the current data for direct sample comparison. The long-term durability of Cu–Fe–NC-3 was evaluated by cycling 2000 times at a scanning rate of 50 mV s^{-1} in O_2- saturated 0.1 M KOH solution, within the potential range of 0.6 to 1.2 V.

The electron transfer number (n) was evaluated based on the eqn (S1)–(S3) in the ESI.†

Results and discussion

Structure and morphology characterization

The XRD patterns of Cu–C–N, Fe–C–N, and Cu–Fe–CN-3 samples before and after acid treatment are illustrated in Fig. 2a. After acid treatment, the characteristic peak strengths of Cu–C–N, Fe–C–N, and Cu–Fe–CN-3 samples become very weak, indicating that most nanoparticles are removed. The Cu–Fe–CN-3 catalyst exhibits additional peaks corresponding to Fe (JCPDS no. 06-0696) and Cu (JCPDS no. 04-0836). Based on N_2 adsorption–desorption experiment, BET surface areas for BP2000-acid, Fe–C–N, Cu–C–N, and Cu–Fe–CN-3 were measured as 713, 576, 521, and 411 m^2 g^{-1}, respectively (ESI, Fig. S1†). The significant decrease in the surface area of Cu–Fe–CN-3 can be attributed to the agglomeration of Fe and Cu nanoparticles, resulting from the introduction of iron and copper sources during the pyrolysis. The Cu–C–N, Fe–C–N, and Cu–Fe–CN-3 of the acid-washed sample exhibit two broad peaks at 2θ values of approximately 24.8° and 42.9°, which are significantly widened due to the presence of amorphous carbon. Due to their weak

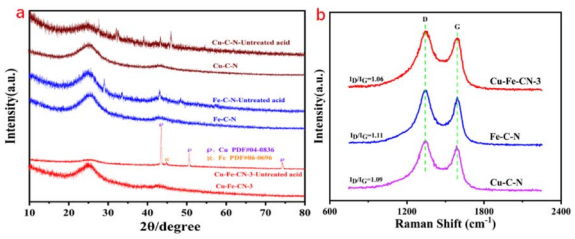

Fig. 2 (a) XRD patterns of Fe–C–N, Cu–C–N, and Cu–Fe–NC-3 before and after acid treatment. (b) Raman spectra of Cu–C–N, Fe–C–N, and Cu–Fe–CN-3.

intensity and limited number, it is challenging to precisely determine the specific metallic structure associated with these diffraction peaks. We can only speculate that they may correspond to iron-nitrogen, copper-nitrogen, carbide, and graphite peaks.[33–35] Further confirmation through additional XPS characterization is necessary. Furthermore, the Raman spectra of Cu–C–N, Fe–C–N, and Cu–Fe–CN-3 typically exhibit two broad signals corresponding to the D-band and G-band of graphite at approximately 1344 cm^{-1} and 1592 cm^{-1}, respectively. The calculated I_D/I_G values for Cu–C–N, Fe–C–N, and Cu–Fe–CN-3 catalyst samples were found to be 1.09, 1.11, and 1.06, respectively. The aforementioned observation further demonstrates that the sample containing both Fe and Cu (Cu–Fe–CN-3) exhibits the highest degree of graphitization. It is worth noting that a higher degree of graphitization promotes an increased charge transfer, which may also account for its superior ORR activity.[11,22,28] These findings sufficiently support the notion that transition metal doping facilitates the process of carbon material graphitization, leading to a partial hybridization of sp^3 to sp^2 carbon structure, which is in agreement with the XRD data presented in Fig. 2a. The SEM images of the Cu–Fe–CN-3 electrocatalyst in Fig. 3a reveal the presence of a series of spherical carbon particles resembling pearls. However, it is challenging to discern the presence of iron and copper in these low-resolution images shown in Fig. 3b. High-resolution TEM images verified that no obvious crystalline metal nanoparticles or clusters were formed in the carbon matrix (Fig. 3c). Fe and Cu in the Cu–Fe–CN-3 sample are shown as black dots embedded on the carbon surface (inside the red circle), and obvious single Fe and Cu atoms could be observed. Cu–C–N and Fe–C–N samples, like SEM images of the Cu–Fe–CN-3 electrocatalyst, showed the presence of a series of pearl-like spherical carbon particles (ESI, Fig. S2(a and b)†). It is also difficult to discern the presence of iron and copper in low-resolution images (ESI, Fig. S2(c and d)†). High-resolution TEM images confirmed that both Cu–C–N and Fe–C–N electrocatalysts, similar to the Cu–Fe–CN-3 samples, exhibited atomic nesting on the carbon surface (inside the red circle), allowing for individual observation of Fe and Cu atoms (ESI, Fig. S2(e and f)†). The element mapping shows that Cu (green), Fe (red), C (blue), N (purple), and O (yellow) are uniformly distributed in the resulting Cu–Fe–CN-3 catalyst (Fig. 3d–i). Furthermore, no peaks corresponding to crystalline iron or copper groups or metal carbide nanoparticles were detected in the XRD analysis of the Cu–Fe–CN-3 samples. These findings are consistent with those obtained from TEM characterization. The excellent contact between Cu and Fe elements on BP2000 carbon enhances the density of accessible active sites, resulting in a superior synergistic promotion effect and enhanced electrocatalytic activity for ORR.

The chemical composition of the Cu–Fe–CN-3 electrocatalyst sample was analyzed using XPS. The high-resolution XPS spectrum (ESI, Fig. S3†) shows that the contents of C (283.55 eV), N (395.00 eV), O (529.00 eV), Fe (706.00 eV), and Cu (930.00 eV) on the surface of the Cu–Fe–CN-3 catalyst are 84.29 at%, 5.54 at%, 7.15 at%, 1.71 at%, and 1.31 at%, respectively. High-resolution XPS spectra (Fig. 4a) show that the C 1s peak consists of C–C (282.1 eV), C–N (282.5 eV), and C–O (283.4 eV). This indicates that the N element is also successfully doped into the carbon material. Fig. 4b shows the XPS spectrum of N 1s. The deconvolution N 1s can be divided into three peaks: iron nitrides (396.1 eV), pyridinic-N and Cu–N (397.3 eV), and pyrrolic-N (398.7 eV). Note that pyridinic-N, Cu–N, and Fe–N components in Cu–Fe–CN-3 samples should include a contribution from N bound to Fe (Fe–N) due to the small difference between the binding energies of Fe–N, Cu–N, and pyridinic N.[18,36] The decrease in the intermediate peak of N 1s may primarily be attributed to the defects present in the matrix deposited by Fe and N on the carbon surface, as well as the elution of its unstable structure.[37] Among them, pyridine-N and pyrrole-N are considered to be active N substances with high ORR activity. The calculations based on density functional theory (DFT), which have been previously reported, indicate that carbon nanostructures containing pyridine N exhibit Lewis basicity.[38] The occupation region near the Fermi level has also been reported to exhibit local state densities for carbon atoms adjacent to the pyridinic N.[39] The presence of electron pairs in carbon atoms allows them to exhibit Lewis base properties, as evidenced by experimental observations.[40] The attachment of oxygen molecules to Lewis bases is

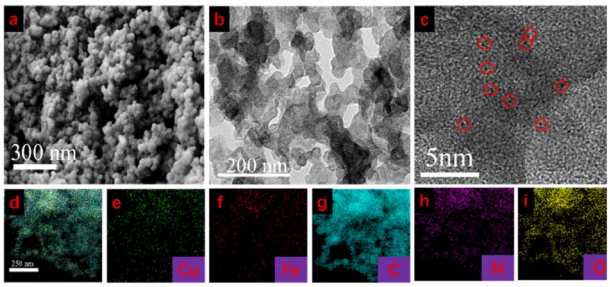

Fig. 3 (a) SEM images, (b) TEM images, (c) HR-TEM images, and (d–i) elemental mapping images of Cu–Fe–CN-3 catalyst samples.

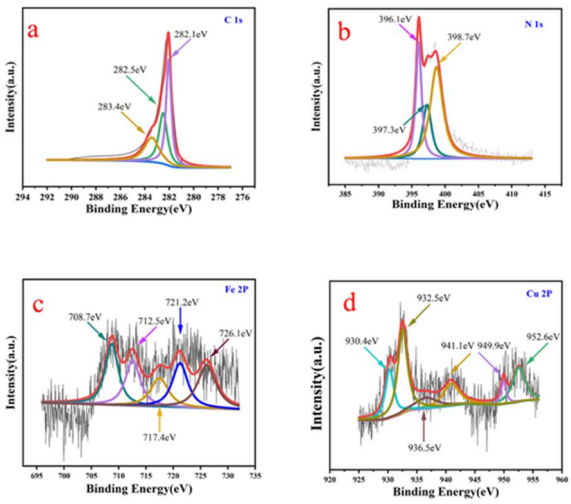

Fig. 4 XPS spectra of (a) C 1s, (b) N 1s, (c) Fe 2p, and (d) Cu 2p for Cu–Fe–CN-3 electrocatalysts.

a widely recognized phenomenon.[41] Since O_2 adsorption is the first step of ORR, the Lewis base produced by pyridine nitrogen is considered to be the active site of ORR.[22,40,42] In the case of Fe 2p spectra (Fig. 4c), the peaks at 708.7 eV, 721.2 eV, 712.5 eV (726.1 eV) are assigned to metallic Fe and Fe^{2+}, Fe^{3+} oxidation state or Fe–N, respectively, with a satellite peak at 717.4 eV, which are consistent with previous literature.[28,33,43,44] From the relative intensity, it is found that metallic Fe is predominant in the sample after ORR. This means that most metallic Fe is stably doped in N-doped Fe-incorporating BP2000. The stable metallic Fe species are contained inside the samples. The existence of Fe inside the samples are also observed in XPS measurements with etched sample surfaces. These results suggest that Fe and Fe–N inside the samples further promote ORR activity associated with the surface Fe–N, although the detailed mechanism is not yet clear. As shown in Fig. 4d, the Cu 2p XPS spectrum of the Cu–Fe–CN-3 sample can be divided into Cu $2p_{3/2}$ (Cu^0 or Cu^+ at 932.5 eV and Cu^{2+} at 936.5 eV), Cu $2p_{1/2}$ (Cu^0 at 952.6 eV), and three satellite peaks at 941.0 eV and 949.9 eV, respectively. The appearance of the Cu 2p satellite peak is related to the unfilled electronic state of Cu 3d° orbit and also indicates the formation of Cu(II) species. High-resolution Cu 2p XPS spectra further disclose that the surficial Cu element of Cu–Fe–CN-3 exists in multiple valences, including Cu(0), Cu(I), and Cu(II).[45] The detection of Cu (0) species agrees well with the observation of XRD peaks of metallic copper in Cu–Fe–CN-3. The Cu(I/II) species might coordinate with the doped N atoms to generate Cu(I/II)–N_x active sites, which is also explained by high-resolution N 1s XPS spectra. The existence of redox electron pair Cu^{2+}/Cu^+ exhibited a perfect catalytic property due to its transformation of oxidation state and reduction state in the oxygen reduction process, which could improve the ORR activity. This finding is consistent with previous reports on monatomic copper catalysts.[25,46–48] It has been discovered that unsaturated Cu–N structures effectively catalyze ORR.

Electrocatalytic performance

The catalytic activity of bimetallic catalysts is critically influenced by the ratio between the two metals, thereby determining the structure and composition of the catalytic active site. By adjusting the Cu to Fe molar ratio in the raw material (as shown in ESI, Fig. S4†), we investigated the impact of this molar ratio on catalytic activity for the linear sweeping voltammograms (LSVs) at 1600 rpm in O_2-saturated 0.1 M KOH recorded on RRDE. The catalyst Cu–Fe–CN-3 with a Cu to Fe molar ratio of 3 : 1 demonstrates the highest peak ORR current potential among other proportional catalysts. The half-wave potential of the catalyst is approximately 0.692 V, 0.867 V, 0.688 V, 0.698 V, 0.722 V, and 0.745 V when the molar ratio of Cu to Fe in the precursor material is adjusted to 4 : 1, 3 : 1, 2 : 1, 1 : 1, 1 : 2, and 1 : 3, respectively. It should be noted that the half-wave potential of Cu–Fe–CN-3 is 0.867 V, which is higher than others due to Fe–N in Fe–N-doped BP2000. However, BP2000 alone does not exhibit significant ORR activity. Thus, it is suggested that Fe or metallic Fe inside the samples promotes the ORR activity due to Fe–N on the surface. Namely, metallic Fe inside the samples gives rise to a synergy effect for the ORR activity with Fe–N on the surface. At the same time, the optimal synergy between Cu and Fe binding is observed when the atomic number ratio is 3 : 1. The effect of varying molar ratios of Cu and Fe on ORR was further investigated through the utilization of cyclic voltammetry in 0.1 M KOH solution saturated with O_2 at 10 mV s^{-1}. It is evident that Cu–Fe–CN-3, Cu–Fe–CN-1/3, Cu–Fe–CN-1/2, Cu–Fe–CN-1, Cu–Fe–CN-4, and Cu–Fe–CN-2 exhibit distinct oxygen reduction peaks (as depicted in ESI, Fig. S5†), which are measured to be 0.896 V, 0.795 V, 0.779 V, 0.771 V, 0.763 V, and 0.752 V, respectively. The results obtained from LSVs and CVs are consistent, thereby optimizing the most suitable Cu to Fe molar ratio of raw materials. In order to further elucidate the advantages of bimetallic catalyst composites, comparative experiments using different materials were conducted, with the corresponding results presented in Fig. 5a. The LSV curve demonstrates the significant electrocatalytic activity of Cu–Fe–CN-3, exhibiting half-wave potential ($E_{1/2}$) of 0.867 V and diffusion-limited current density of −5.79 mA cm^{-2}, surpassing that of commercial Pt/C (0.841 V, −5.21 mA cm^{-2}). Furthermore, we investigated the impact of different materials on the properties by incorporating $Cu(C_5H_7O_2)_2$, $Fe(C_5H_7O_2)_3$, or BP2000-acid. The absence of metal in the catalyst results in low activity for ORR, whereas the incorporation of Cu and/or Fe

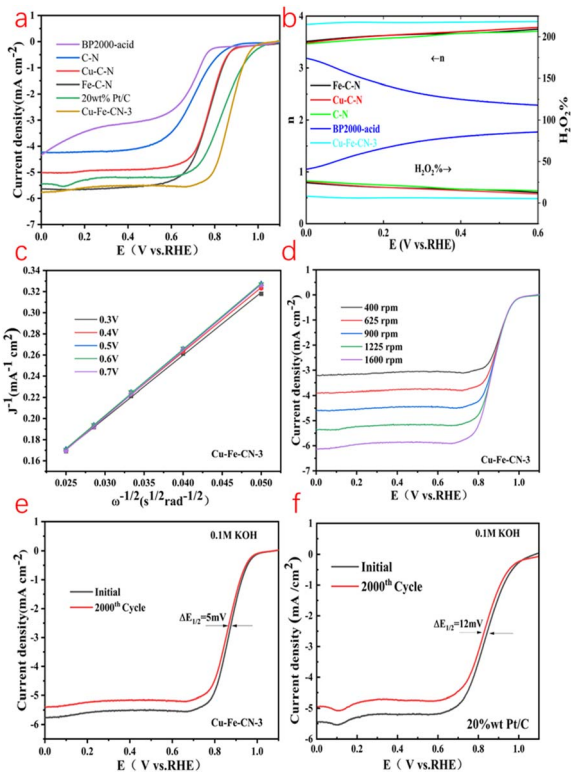

Fig. 5 (a) ORR polarization curves of different catalysts at 1600 rpm. (b) The electron transfer number and percentage of peroxide of different catalysts at different potentials, the RDE in O_2-saturated 0.1 M KOH solution at different rotation rates, and the corresponding Koutecky–Levich plots at different potentials of (c) and (d) Cu–Fe–CN-3, the ORR LSV curves of Cu–Fe–CN-3 and commercial Pt/C before and after 2000 cycles are represented by (e) and (f), respectively.

metals significantly enhances the catalytic performance. Among all samples examined, Cu–Fe–CN-3 exhibited more positive half-wave potential for ORR in O_2-saturated 0.1 M KOH, surpassing that of Cu–C–N (0.777 V), Fe–C–N (0.767 V), C–N (0.701 V), and BP2000-acid (0.658 V). We have adopted a previous pickling purification method to pre-treat the BP2000 carbon (Cabot Corporation),[9,32,49] which differs from the treatment method reported in the current literature.[50,51] Specifically, this method introduces oxygen-containing functional groups on the surface of BP2000-acid while eliminating impurities, thereby enhancing its potential for application in oxygen reduction reactions and providing a higher potential for the final bimetallic catalyst. The cyclic voltammetry (CV) curves of different synthesized catalysts (ESI, Fig. S6†) were evaluated in O_2-saturated 0.1 M KOH solution at a scanning rate of 10 mV s^{-1}, respectively. The results demonstrate that all catalysts exhibit distinct cathodic peaks associated with ORR, indicating their significant electrocatalytic activity towards ORR. Notably, the Cu–Fe–CN-3 catalyst displays a significantly higher peak potential compared to other catalysts, suggesting a remarkable enhancement in ORR performance attributed to the co-introduction of Cu and Fe. The Fe–C–N and Cu–C–N materials exhibit favorable surface areas (as indicated by the BET data above) and possess high electrocatalytic activity towards ORR, suggesting that the Fe–N_x and Cu–N_x structures serve as the primary active sites.[11,35] Although Fe–C–N and Cu–C–N materials possess higher specific surface area than Cu–Fe–CN-3, their ORR activity is inferior to the latter. This implies that the introduction of both Cu and Fe into the composite material leads to an increased exposure of active sites, resulting in an effective synergistic effect between Fe and Cu.[27,52] The final sample of Cu–Fe–NC-3 underwent additional elemental analysis using ICP, revealing a Fe content of 2.6 wt% and Cu content of 3.68 wt%. Furthermore, Raman data indicate that Cu–Fe–CN-3 exhibits a higher degree of graphitization with a relatively complete formation of catalytic active sites, thereby further confirming its superior ORR activity and providing a highly favorable four-electron pathway for efficient ORR.

The calculation reveals that the Tafel slope of Cu–Fe–CN-3 is 69 mV dec^{-1}, which is comparatively lower than Fe–C–N (91 mV dec^{-1}), Cu–C–N (99 mV dec^{-1}), and Pt/C (94 mV dec^{-1}), indicating a higher kinetic efficiency of the Cu–Fe–CN-3 catalyst (ESI, Fig. S7†). To comprehend the electron transfer pathway of diverse catalysts, pertinent data were gathered and computed by employing the rotating ring disk electrode (RRDE) (Fig. 5b). The average yield of H_2O_2 from carbon remains at 70%, while the average number of electron transfers is determined to be 2.3, indicating that the ORR process follows a two-electron pathway. The H_2O_2 yield of other materials except Cu–Fe–CN-3 remains approximately at 10%, while the electron transfer number ranges between 3.6 and 3.9. The Cu–Fe–CN-3 catalyst exhibited a H_2O_2 yield below 10% and an electron transfer number of 3.9, indicating it is beneficial to the $4e^-$ pathway during ORR. In order to further validate the electron transfer mechanism, the reaction pathways of each catalyst were investigated by collecting LSV curves on the RDE at various rotational speeds. Subsequently, the corresponding K–L diagram and electron transfer number (n) were obtained (as shown in ESI, Fig. S8(a–f†), and Fig. 5(c, and d)). The electron transfer numbers of Cu–Fe–CN-3, Fe–C–N, Cu–C–N, and BP2000-acid are 3.9, 3.8, 3.7, and 2.1, respectively. This indicates that the prepared Cu–Fe–CN-3 target material promotes a four-electron transfer process in the overall reaction and exhibits high catalytic efficiency for ORR. The performance of the catalyst was also compared with that reported in recent literature, demonstrating a certain level of competitiveness (Table 1). More importantly, considering practical applications, the long-term stability of Cu–Fe–CN-3 and the Pt/C catalysts is a crucial factor influencing ORR. The electrochemical durability of the catalysts was assessed through an accelerated polarization cycling durability test conducted in an O_2-saturated 0.1 M KOH solution within the potential range of 0–1.1 V (*vs.* RHE), as depicted in Fig. 5e and f. After 2000 cycles, $E_{1/2}$ of the Cu–Fe–CN-3 catalyst exhibits a slight negative shift by 5 mV, which is better than the activity loss of Cu–C–N (8 mV) (ESI, Fig. S9†), Fe–C–N (10 mV) (ESI, Fig. S10†), and Pt/C catalyst (12 mV), thereby indicating superior long-term stability for ORR. The binding mode of Pt nanoparticles with carbon is an important factor affecting the decline in activity of the Pt/C catalyst. In the case of Cu–Fe–CN-3, the strong synergistic interactions between stable Cu–N_x and Fe–N_x groups and carbon carriers contribute significantly to the structural stability of Cu–Fe–CN-3.

The ORR process typically comprises the following four fundamental electronic steps:[56,57]

$$O_2^* + H + e^- \rightarrow OOH^*$$

$$OOH^* + H^+ + e^- \rightarrow O^* + H_2O$$

$$O^* + H^+ + e^- \rightarrow OH^*$$

$$OH^* + H^+ + e^- \rightarrow H_2O^*$$

Table 1 The comparative evaluation of ORR properties of various non-noble metal catalysts in alkaline media

Sample	E_{onset}/V	$E_{1/2}$/V	J_L/mA cm^{-2}	H_2O_2/%	n	Ref.
FeCu@C–N	0.987	0.864	~6.2	<5	~4.0	1
CuNDs/Fe_2O_3–NPCs	0.98	0.85	6.5	8.9	3.78	43
FeCu SACs/NC	1.03	0.89	7.63	2.6	3.95	52
FeCo–NC-3	0.982	0.842	—	—	~4	53
Co‖Cu/NC		0.83	5.8	10.3	3.9	54
$Fe_{0.25}Co_{0.75}$/NC	0.99 V	0.86	6.01	<5	3.9	55
Cu–Fe–CN-3	1.01	0.867	5.79	<10	3.9	This work

where * indicates the reaction site; OOH*, O*, and OH* are adsorption intermediates. The adsorption of O_2 is a non-electrochemical process.

The redox coupling exerts an influence on the electronic properties of the catalyst surface, primarily evidenced by alterations in binding energy and electrocatalytic activity at the active site.[52,58] The partial electron density of states of Fe and Cu is distributed throughout the Cu–Fe–CN-3 structure, thereby providing ample active sites for catalyzing oxygen reduction.[59] According to the latest reports, the density of states of the Fe (d-orbital) near the Fermi level is higher than that of Cu.[52,60,61] The significantly elevated electron density on Fe hampers the adsorption of intermediate substances in oxygen reduction. The oxygen adsorption capacity of Cu is superior to that of Fe, whereas the interaction between Fe and reactive oxygen species exhibits greater strength. The strong electron transfer from Cu to Fe facilitates the alignment of the d-band center with the Fermi level, thereby promoting the dynamic splitting of the O–O band on the Cu surface and enhancing dissociation activity. Moreover, the electron-enriched state resulting from strong electron transfer facilitates the adsorption of Fe, thereby promoting the generation of excessive reactive oxygen species on the Cu surface.[25] The catalytic reduction of oxygen by different single-atom Cu and Fe species can be observed to proceed *via* a four-electron reaction.[62] The strong electron transfer from Cu to Fe facilitates the rapid dissociation of O–O on the Cu surface, leading to the generation of reactive oxygen species that promptly bind with Fe upon splitting.[60] The findings imply that this distinctive electronic interaction in bimetallic site catalysts presents novel prospects for enhancing the efficiency of catalysts devoid of precious metals, particularly in fuel cells, metal–air batteries, and other renewable energy systems.

Catalytic performance for Al–air battery

The outstanding ORR performance prompted us to evaluate the actual performance of Cu–Fe–CN-3 and 20% Pt/C catalysts in a laboratory-made Al–air battery. The aforementioned two catalysts are loaded onto the Ni foam as an air cathode, Al plate as an anode, 6 M KOH as an electrolyte, and additional additives are incorporated to mitigate accelerated corrosion of the aluminum plate. As can be seen from Fig. 6a–c, the discharge voltage of all batteries initially exhibited a gradual increase over time. This can be attributed to the progressive dissolution of the passivation film on the surface of the aluminum anode, which is caused by the early activation process. The devices equipped with Cu–Fe–CN-3 catalyst were tested at current densities of 20 mA cm^{-2}, 50 mA cm^{-2}, and 100 mA cm^{-2}, and the corresponding average voltages are 1.56 V, 1.37 V, and 1.12 V, respectively. In comparison, the average voltage recorded for commercial Pt/C at the corresponding current density is 1.48 V, 1.25 V, and 0.96 V, respectively. It can be seen from the above data that the difference between Cu–Fe–CN-3 and commercial Pt/C becomes larger with the increasing current density. The Cu–Fe–CN-3 catalyst exhibits exceptional catalytic performance, suggesting its potential to replace the costly precious metal Pt/C as an ORR catalyst for Al–air batteries.

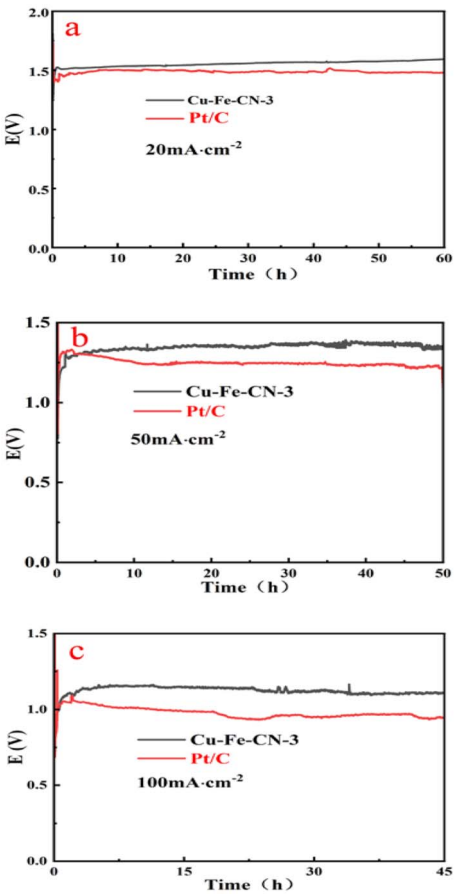

Fig. 6 Full-cell test of catalysts. Discharge profiles (a, b, and c) of Cu–Fe–CN-3 electrocatalyst and the commercial Pt/C at various current densities in Al–air batteries.

Conclusions

In summary, the focus of this study lies in the development of a straightforward and efficient strategy for synthesizing high-performance Cu–Fe–CN-3 electrocatalysts. After the incorporation of Cu and Fe elements into Black Pearls' carbon black, the synergistic effect between Fe and Cu enhances the exposure of active sites for ORR and facilitates the electron transfer of substances related to ORR. In addition, the structural stability of Cu–Fe–CN-3 is enhanced by the strong interaction between stable Cu–N_x and Fe–N_x groups with carbon carriers. The synthesized catalyst demonstrates a four-electron transfer pathway in ORR equivalent to that of commercially available Pt/C. The Cu–Fe–CN-3 catalyst exhibits exceptional performance in metal fuel cells, surpassing that of commercial platinum carbon when tested under identical current density conditions. The Cu–Fe–CN-3 electrocatalysts, serving as a promising cathode catalyst, exhibit significant potential for the development of cost-effective and highly efficient electrocatalysts in proton exchange membrane fuel cells, aluminum–air cells, zinc–air cells, and magnesium–air cells. However, during the discharge process of alkaline aluminum–air batteries, the aluminum alloy anode initially undergoes a reaction with OH^- to form a soluble

compound, which subsequently transforms into a gel-like $Al(OH)_3$ precipitate over time. The accumulation of this hydrated $Al(OH)_3$ colloidal product on the electrode leads to anode passivation. As it continues to accumulate, resistance increases significantly, and polarization becomes severe, resulting in a drop in working voltage and promoting further precipitation of $Al(OH)_3$. To address this issue, additional additives can be introduced in subsequent studies to enhance performance.

Author contributions

Kun Liu: data curation, methodology, investigation, visualization, writing-original draft. Xiaoyue Ye: conceptualization, investigation, formal analysis. Angli Zhang: data curation, software, validation, visualization. Xiaoyan Wang: resources, supervision. Ting Liang: methodology. Yan Fang: conceptualization, supervision. Wang Zhang: project administration, validation. Ke Hu: validation, visualization. Xiaowu Liu: writing-review & editing, funding acquisition. Xin Chen: supervision, resources, writing-review & editing, funding acquisition.

Conflicts of interest

The authors declare that they have no known competing financial interests or personal relationships that could have appeared to influence the work reported in this paper.

Acknowledgements

This work was financially supported by the Excellent Research and Innovation Team Project of Anhui Province (2023AH010077), the Key Project of Education Department of Anhui Province (2022AH051679 and 2022AH051686), the Scientific Research Foundation for High-Level Talents of West Anhui University (WGKQ202001001 and WGKQ202001003), and Outstanding Young Backbone Teachers in Colleges and Universities Visit and Study Projects in China (gxgnfx2022050).

Notes and references

1 J. Li, J. Chen, H. Wan, J. Xiao, Y. Tang, M. Liu and H. Wang, *Appl. Catal., B*, 2019, **242**, 209–217.
2 S. Zhang, Y. Wang, Y. Li, M. Wei and K. Wang, *ACS Appl. Energy Mater.*, 2022, **5**, 15909–15917.
3 A. A. Nada, A. Opálková Šišková, A. Kleinová, A. E. Andicsová, E. Šimon and J. Mosnáček, *J. Power Sources*, 2023, **572**, 233089–233098.
4 H. Wen, Z. Liu, J. Qiao, R. Chen, R. Zhao, J. Wu, G. Qiao and J. Yang, *Int. J. Energy Res.*, 2020, **44**, 7568–7579.
5 S. M. A. Nayem, S. Islam, M. Mohamed, S. Shaheen Shah, A. J. S. Ahammad and M. A. Aziz, *Chem. Rec.*, 2024, **24**, e202300005–e202300034.
6 M. Bonechi, W. Giurlani, M. Vizza, M. Savastano, A. Stefani, A. Bianchi, C. Fontanesi and M. Innocenti, *Catalysts*, 2021, **11**, 764–772.
7 P. Goel, D. Dobhal and R. C. Sharma, *J. Energy Storage*, 2020, **28**, 101287–101298.
8 K. Liu, X. Huang, H. Wang, F. Li, Y. Tang, J. Li and M. Shao, *ACS Appl. Mater. Interfaces*, 2016, **8**, 34422–34430.
9 J. Li, Z. Zhou, K. Liu, F. Li, Z. Peng, Y. Tang and H. Wang, *J. Power Sources*, 2017, **343**, 30–38.
10 K. Liu, Z. Peng, H. Wang, Y. Ren, D. Liu, J. Li, Y. Tang and N. Zhang, *J. Electrochem. Soc.*, 2017, **164**, F475–F483.
11 M. J. Kim, S. Kim, J. E. Park, C. C. Hwang, S. Lee, S. Y. Kang, D. Jung, Y. H. Cho, J. Kim, K. S. Lee and Y. E. Sung, *Nano Energy*, 2020, **78**, 105395–105405.
12 B. Liu, B. Huang, C. Lin, J. Ye and L. Ouyang, *Appl. Surf. Sci.*, 2017, **411**, 487–493.
13 X. Zhang, X. Hu, S. Lv, Y. Li, J. Ren and Y. Huang, *Int. J. Hydrogen Energy*, 2021, **46**, 38692–38700.
14 X. Wang, J. Du, Q. Zhang, L. Gu, L. Cao and H.-P. Liang, *Carbon*, 2020, **157**, 614–621.
15 H. Xu, D. Wang, P. Yang, A. Liu, R. Li, Y. Li, L. Xiao, X. Ren, J. Zhang and M. An, *J. Mater. Chem. A*, 2020, **8**, 23187–23201.
16 Z. Liang, H. Zheng and R. Cao, *ChemElectroChem*, 2019, **6**, 2600–2614.
17 Z. Chen, W. Gong, Z. Liu, S. Cong, Z. Zheng, Z. Wang, W. Zhang, J. Ma, H. Yu, G. Li, W. Lu, W. Ren and Z. Zhao, *Nano Energy*, 2019, **60**, 394–403.
18 Y. Zheng, H. Song, S. Chen, X. Yu, J. Zhu, J. Xu, K. A. I. Zhang, C. Zhang and T. Liu, *Small*, 2020, **16**, 2004342–2004353.
19 J. Zhang, A. Yu and C. Sun, *Appl. Surf. Sci.*, 2022, **605**, 154534–154541.
20 G. Xiao, R. Lu, J. Liu, X. Liao, Z. Wang and Y. Zhao, *Nano Res.*, 2021, **15**, 3073–3081.
21 X. Liu, P. Xu, Q. Fu, R. Li, C. He, W. Yao, L. Wang, S. Xie, Z. Xie, Q. He and J. C. Crittenden, *Chem. Eng. J.*, 2021, **426**, 131679–131690.
22 S. Liu, H. Yang, L. Yao, H. Peng, P. Huang, X. Lin, L. Liu, H. Zhang, P. Cai, X. Wen, Y. Zou, C. Xiang, F. Xu, L. Sun, P. Kannan and S. Ji, *Int. J. Hydrogen Energy*, 2022, **47**, 7751–7760.
23 X. X. Wang, D. A. Cullen, Y. T. Pan, S. Hwang, M. Wang, Z. Feng, J. Wang, M. H. Engelhard, H. Zhang, Y. He, Y. Shao, D. Su, K. L. More, J. S. Spendelow and G. Wu, *Adv. Mater.*, 2018, **30**, 1706758–1706769.
24 D. E. Beltrán and S. Litster, *ACS Energy Lett.*, 2019, **4**, 1158–1161.
25 X. L. Chen, L. S. Ma, W. Y. Su, L. F. Ding, H. B. Zhu and H. Yang, *Electrochim. Acta*, 2020, **331**, 135273–135283.
26 A. Onoda, Y. Tanaka, K. Matsumoto, M. Ito, T. Sakata, H. Yasuda and T. Hayashi, *RSC Adv.*, 2018, **8**, 2892–2899.
27 Y. S. Kang, Y. Heo, J. Y. Jung, Y. Sohn, S. H. Lee, J. H. Jang, P. Kim and S. J. Yoo, *J. Ind. Eng. Chem.*, 2019, **71**, 234–241.
28 J. Ma, D. Duan, W. Gao, F. Hu, S. Liu, W. Su, H. Peng, K. Zhang, F. Xu and L. Sun, *Electrocatalysis*, 2021, **12**, 362–371.
29 X. L. Wang, L. Z. Dong, M. Qiao, Y. J. Tang, J. Liu, Y. Li, S. L. Li, J. X. Su and Y. Q. Lan, *Angew. Chem., Int. Ed.*, 2018, **57**, 9660–9664.

30 S. Muthusamy, A. Sabbah, P. Sabhapathy, Y. C. Chang, T. Billo, Z. Syum, L. C. Chen and K. H. Chen, *ChemElectroChem*, 2023, **10**, e202300272–e202300283.
31 P. Sabhapathy, P. Raghunath, A. Sabbah, I. Shown, K. S. Bayikadi, R. K. Xie, V. Krishnamoorthy, M. C. Lin, K. H. Chen and L. C. Chen, *Small*, 2023, **19**, 2303598–2303608.
32 D. Liu, L. Fu, X. Huang, K. Liu, J. Li, H. Xie, H. Wang and Y. Tang, *J. Electrochem. Soc.*, 2018, **165**, F662–F670.
33 Y. Qiao, Y. Ni, F. Kong, R. Li, C. Zhang, A. Kong and Y. Shan, *Chem.–Asian J.*, 2019, **14**, 2676–2684.
34 D. Shin, M. Choun, H. C. Ham, J. K. Lee and J. Lee, *Phys. Chem. Chem. Phys.*, 2017, **19**, 21987–21995.
35 X. Xie, J. Liu, T. Li, Y. Song and F. Wang, *Chem.–Eur. J.*, 2018, **24**, 9968–9975.
36 N. Kumari, A. Kumar, V. K. V. P. Srirapu and R. N. Singh, *Int. J. Hydrogen Energy*, 2018, **43**, 1781–1789.
37 X. Yang, Y. Wang, G. Zhang, L. Du, L. Yang, M. Markiewicz, J. y. Choi, R. Chenitz and S. Sun, *Appl. Catal., B*, 2020, **264**, 118523–118531.
38 B. Li, X. Sun and D. Su, *Phys. Chem. Chem. Phys.*, 2015, **17**, 6691–6694.
39 T. Kondo, S. Casolo, T. Suzuki, T. Shikano, M. Sakurai, Y. Harada, M. Saito, M. Oshima, M. I. Trioni, G. F. Tantardini and J. Nakamura, *Phys. Rev. B*, 2012, **86**, 035436–035442.
40 D. Guo, R. Shibuya, C. Akiba, S. Saji, T. Kondo and J. Nakamura, *Science*, 2016, **351**(6271), 361–365.
41 H. Metiu, S. Chrétien, Z. Hu, B. Li and X. Sun, *J. Phys. Chem. C*, 2012, **116**, 10439–10450.
42 W. Ding, L. Li, K. Xiong, Y. Wang, W. Li, Y. Nie, S. Chen, X. Qi and Z. Wei, *J. Am. Chem. Soc.*, 2015, **137**, 5414–5420.
43 Q. Dong, H. Wang, J. Ren, X. Wang and R. Wang, *Chem. Eng. J.*, 2022, **442**, 136128–136137.
44 X. Li, B. Zhang, X. Yan, Y. Zhang, X. Deng and S. Zhang, *Catal. Today*, 2019, **337**, 97–101.
45 M. Mosaferi, P. Selles, T. Miteva, A. Ferté and S. Carniato, *J. Phys. Chem. A*, 2022, **126**, 4902–4914.
46 S. Xie, L. Li, Y. Chen, J. Fan, Q. Li, Y. Min and Q. Xu, *ACS Appl. Mater. Interfaces*, 2021, **13**, 3949–3958.
47 M. Zhong, C. Ren, D. Fang, C. Lv and K. Li, *J. Electroanal. Chem.*, 2020, **878**, 114570–114577.
48 Z. Wang, P. Tian, H. Zhang, K. Deng, H. Yu, Y. Xu, X. Li, H. Wang and L. Wang, *Inorg. Chem.*, 2023, **62**, 5622–5629.
49 J. Chen, N. Zhou, H. Wang, Z. Peng, H. Li, Y. Tang and K. Liu, *Chem. Commun.*, 2015, **51**, 10123–10126.
50 R. S. Ribeiro, M. Florent, J. J. Delgado, M. F. R. Pereira and T. J. Bandosz, *Nanoscale*, 2023, **15**, 18592–18602.
51 G. de Falco, M. Florent and T. J. Bandosz, *Carbon*, 2022, **189**, 230–239.
52 H. Liu, L. Jiang, Y. Wang, X. Wang, J. Khan, Y. Zhu, J. Xiao, L. Li and L. Han, *Chem. Eng. J.*, 2023, **452**, 138938–138946.
53 Y. b. Chen, J. j. Li, Y. p. Zhu, J. Zou, H. Zhao, C. Chen, Q.-q. Cheng, B. Yang, L. l. Zou, Z. q. Zou and H. Yang, *J. Mater. Chem. A*, 2022, **10**, 9886–9891.
54 J. Cai, X. Zhang, Y. Shi, Y. Ye and S. Lin, *ACS Sustain. Chem. Eng.*, 2022, **10**, 5986–5997.
55 G. Zhu, H. Yang, Y. Jiang, Z. Sun, X. Li, J. Yang, H. Wang, R. Zou, W. Jiang, P. Qiu and W. Luo, *Adv. Sci.*, 2022, **9**, e2200394–e2200403.
56 L. Zhou, P. Zhou, Y. Zhang, B. Liu, P. Gao and S. Guo, *J. Energy Chem.*, 2021, **55**, 355–360.
57 J. W. Chen, S. Y. Wu and H. T. Chen, *Int. J. Energy Res.*, 2021, **46**, 1032–1042.
58 C. Goswami, H. Saikia, B. Jyoti Borah, M. Jyoti Kalita, K. Tada, S. Tanaka and P. Bharali, *J. Colloid Interface Sci.*, 2021, **587**, 446–456.
59 T. Morishita, T. Ueno, G. Panomsuwan, J. Hieda, M. A. Bratescu and N. Saito, *J. Phys. D: Appl. Phys.*, 2016, **49**, 415305–415310.
60 H. Li, H. Shi, Y. Dai, H. You, S. Raj Babu Arulmani, H. Zhang, C. Feng, L. Huang, T. Zeng, J. Yan and X. Liu, *J. Colloid Interface Sci.*, 2022, **628**, 652–662.
61 S. Yin, Y. Shen, J. Zhang, H. M. Yin, X. Z. Liu and Y. Ding, *Appl. Surf. Sci.*, 2021, **545**, 149042–149050.
62 E. Wang, K. Chen, Y. Chen, J. Zhang, X. Lin and M. Chen, *Sci. China: Chem.*, 2020, **64**, 17–21.